Original Article

MOLECULAR METABOLISM

Liver-specific rescuing of CEACAM1 reverses endothelial and cardiovascular abnormalities in male mice with null deletion of *Ceacam1* gene

Lucia Russo [1,6], Harrison T. Muturi [1,2,6], Hilda E. Ghadieh [1], Alexander M. Wisniewski [1], Eric E. Morgan [1], Syed S. Quadri [4], Gavin P. Landesberg [5], Helmy M. Siragy [4], Guillermo Vazquez [1], Rosario Scalia [5], Rajesh Gupta [1], Sonia M. Najjar [1,2,3,*]

ABSTRACT

Objective: Mice with global null mutation of *Ceacam1* ($Cc1^{-/-}$), display impairment of insulin clearance that causes hyperinsulinemia followed by insulin resistance, elevated hepatic *de novo* lipogenesis, and visceral obesity. In addition, they manifest abnormal vascular permeability and elevated blood pressure. Liver-specific rescuing of Ceacam1 reversed all of the metabolic abnormalities in $Cc1^{-/-liver+}$ mice. The current study examined whether $Cc1^{-/-}$ male mice develop endothelial and cardiac dysfunction and whether this relates to the metabolic abnormalities caused by defective insulin extraction.

Methods and results: Myography studies showed reduction of agonist-stimulated nitric oxide production in resistance arterioles in $Cc1^{-/-}$, but not $Cc1^{-/-liver+}$ mice. Liver-based rescuing of CEACAM1 also attenuated the abnormal endothelial adhesiveness to circulating leukocytes in parallel to reducing plasma endothelin-1 and recovering plasma nitric oxide levels. Echocardiography studies revealed increased septal wall thickness, cardiac hypertrophy and reduced cardiac performance in $Cc1^{-/-}$, but not $Cc1^{-/-xliver+}$ mice. Insulin signaling experiments indicated compromised IRS1/Akt/eNOS pathway leading to lower nitric oxide level, and activated Shc/MAPK pathway leading to more endothelin-1 production in the aortae and hearts of $Cc1^{-/-}$, but not $Cc1^{-/-xliver+}$ mice. The increase in the ratio of endothelin-1 receptor A/B indicated an imbalance in the vasomotor activity of $Cc1^{-/-}$ mice, which was normalized in $Cc1^{-/-xliver+}$ mice.

Conclusions: The data underscore a critical role for impaired CEACAM1-dependent hepatic insulin clearance pathways and resulting hyperinsulinemia and lipid accumulation in aortae and heart in regulating the cardiovascular function.

Keywords Insulin clearance; Hyperinsulinemia; Insulin resistance; Endothelial function; Cardiomyopathy

1. INTRODUCTION

Insulin resistance, heralded by hyperinsulinemia with altered glucose and lipid homeostasis [1] and diminished regulation of nutrient delivery through the microcirculation [2], is linked to endothelial dysfunction [3–5]. In the vascular endothelium, insulin resistance exerts a pro-hypertensive/atherogenic effect by impairing nitric oxide (NO) production, increasing the vasoconstrictor tone through endothelin-1 activity, and inducing the expression of pro-inflammatory cell adhesion molecules, such as vascular cell adhesion molecule-1 (VCAM-1) [5]. Decreased NO bioavailability is accompanied by reduced vasodilation in response to stimuli, such as acetylcholine, and increased leukocyte-endothelium adhesiveness [6], cardinal features of the early phase of endothelial dysfunction commonly seen in atherosclerosis.

Insulin resistance underlies vascular disturbances in humans and rodents [4,7–10]. Heterozygous insulin receptor knockout mice develop systemic insulin resistance with reduced basal and insulin-stimulated NO release [11]. Moreover, ablating insulin receptors in endothelial cells impairs phosphatidylinositol 3-kinase-dependent insulin signaling pathways without affecting glucose homeostasis and blood pressure under basal conditions [12].

The carcinoembryonic antigen-related cell adhesion molecule-1, CEACAM1, is a plasma membrane glycoprotein that undergoes phosphorylation by the insulin receptor [13]. It regulates insulin action by promoting receptor-mediated insulin uptake and degradation in the hepatocyte, the main mechanism of insulin clearance [14]. Consistently, $Cc1^{-/-}$ mice with global deletion of *Ceacam1* exhibit hyperinsulinemia caused by impaired insulin clearance, followed by insulin

[1]Center for Diabetes and Endocrine Research, College of Medicine and Life Sciences, The University of Toledo, Toledo, OH 43614, USA [2]Department of Biomedical Sciences, Heritage College of Osteopathic Medicine, Ohio University, Athens, OH 45701, USA [3]Diabetes Institute, Heritage College of Osteopathic Medicine, Ohio University, Athens, OH 45701, USA [4]Department of Endocrinology and Metabolism, College of Medicine, University of Virginia, Charlottesville, VA, USA [5]Department of Physiology and Cardiovascular Research Center, School of Medicine, Temple University, Philadelphia, PA, USA

[6] Authors contributed equally to the work.

*Corresponding author. Heritage College of Osteopathic Medicine, Office of Grants and Research Irvine Hall, Room 220B, 1, Ohio University, Athens, OH 45701-2979, USA. Fax: +1 740 593 2320. E-mail: najjar@ohio.edu (S.M. Najjar).

Received December 1, 2017 • Revision received January 7, 2018 • Accepted January 14, 2018 • Available online 31 January 2018

https://doi.org/10.1016/j.molmet.2018.01.009

Nonstandard abbreviations used

CEACAM1	Carcinoembryonic antigen-related cell adhesion molecule 1
Ceacam1(Cc1)	Gene encoding CEACAM1 protein
$Cc1^{-/-}$	Global *Ceacam1* null mouse
$Cc1^{-/-xliver+}$	$Cc1^{-/-}$ mouse with liver-specific rescuing of the rat *Ceacam1* gene
ET-1	Endothelin-1
Etar and *Etbr*	mRNA of Endothelin-1 receptor-A and -B
eNOS	Endothelial nitric oxide synthase
FASN	Fatty acid synthase
Icam-1	mRNA of Intercellular cell adhesion molecule-1
IRβ	β subunit of the insulin receptor
m*Cc1*	Mouse *Cc1* gene
NO	Nitric oxide
RAS	Renin–angiotensin–aldosterone system
r*Cc1*	Rat *Cc1* gene
VCAM-1	Vascular cell adhesion molecule-1

resistance, which is systemically manifested at 5–6 months of age when the mice are propagated on the C57BL/6 mice [15,16]. Consistent with the lipogenic effect of hyperinsulinemia [17], $Cc1^{-/-}$ mice exhibit increased hepatic lipid production and redistribution to white adipose tissue and visceral obesity [18]. These metabolic abnormalities were all reversed by liver-specific rescuing of CEACAM1 in $Cc1^{-/-}$ mice [19]. Persistence of insulin resistance in the presence of nicotinic acid, a lipolysis blocker, confirmed that insulin resistance precedes lipolysis, and is mainly driven by chronic hyperinsulinemia that is caused by impaired CEACAM1-dependent insulin clearance pathways in these null mice [19].

In addition to their altered metabolic phenotype, $Cc1^{-/-}$ mice develop endothelial and vascular disturbances, including increased basal vascular permeability [20]. In large vessels, they exhibit low basal NO levels, defective endothelial NO-dependent relaxation of aortic rings in response to acetylcholine, and the development of small intimal plaque-like lesions in the absence of hypercholesterolemia, in addition to fibrosis, increased inflammatory infiltration and leukocytes recruitment to the aorta when fed a standard chow diet at >6 months of age [21]. They also manifest higher systolic blood pressure and activated renin–angiotensin–aldosterone system (RAS) following insulin resistance at 6 months of age [22].

To address the role of impaired hepatic insulin clearance in the pathogenesis of cardiovascular abnormalities, the current studies examined whether global *Ceacam1* deletion causes cardiac and endothelial dysfunctions and whether this is reversed by liver-specific transgenic CEACAM1 reconstitution in order to determine the role of defective hepatic insulin clearance in the pathogenesis of cardiovascular disease.

2. MATERIALS AND METHODS

2.1. Mice generation

The generation of C57BL/6.$Cc1^{-/-xliver+}$ mice harboring rescuing of CEACAM1 exclusively in the liver of $Cc1^{-/-}$ mice has been described [19]. Briefly, $Cc1^{-/-}$ mice [15,16] were crossed with L-CC1 mice with Apolipoprotein A1-driven liver-specific overexpression of wild-type rat *Ceacam1* gene [23]. Intercrossing the progeny produced several genotypes, including those used in these studies: $Cc1^{-/-}$ with the transgene ($Cc1^{-/-xliver+}$) and their control littermates: $Cc1^{-/-}$ and $Cc1^{+/+}$ without the transgene.

Male mice (6–9 months of age) were kept in a 12 h-light/dark cycle and fed *ad libitum* a standard chow diet [23]. Unless otherwise mentioned, mice were anesthetized using an intraperitoneal injection of pentobarbital (1.1 mg/kg BW). At the end of the experiments, mice were euthanized by CO_2 asphyxiation. All procedures were approved by the Institutional Animal Care and Utilization Committee at the University of Toledo College of Medicine and at the Heritage College of Osteopathic Medicine in compliance with the guide for the Care and Use of Laboratory Animals published by the US National Institutes of Health (NIH Publication NO. 85-23, revised 1996, updated 2011).

2.2. Tissue, plasma and urine biochemistry

Plasma was derived from retro-orbital venous blood drawn at 1100 h after an overnight fast [15] to determine levels of insulin (Linco Research), C-peptide (Mouse Ultrasensitive ELISA kit, Alpco), endothelin-1 (ET-1) (Abcam, ELISA ab133030), IL-6 (Abcam, ELISA ab100712), TNFα (Abcam, ELISA ab100747) and prostaglandin 2 (PGE2) (Abcam, ELISA ab133021). Plasma and tissue levels of NO was assessed using a Nitrate/Nitrite Fluorometric Assay Kit (Cayman Chemical, Cat#780051), and fluorescence was measured by the Synergy H1 Hybrid Microplate Reader (BioTek Instruments, Winooski, VT) at 360 nm excitation and 430 nm emission wavelengths. Tissue triacylglycerol level, urine albumin (Albuwell Exocell), and creatinine levels (Cayman) were assessed as described [15,16,22].

2.3. Fatty acid synthase activity

As previously described [19], tissues were homogenized and fatty acid synthase activity (FASN) was measured in the supernatant by adding a reaction mix containing 0.1 μCi [^{14}C] malonyl-CoA (Perkin–Elmer) and 25 nmol malonyl-CoA in the absence or presence of 500 μM NADPH (Sigma–Aldrich) [24]. The reaction was stopped with 1:1 chloroform:methanol solution and samples were centrifuged, butanol-extracted, and counted. FASN activity was calculated as cpm of [^{14}C] incorporated Bq/μg cell lysates.

2.4. Oxidative stress

NADP/NADPH ratio was assessed using Fluorescent NADP/NADPH detection kit (Cell Technology). Fluorescence with excitation at 530 nm and emission at 590 nm was measured using fluorescence plate reader. The concentration was determined using the slope equation generated by the standard. NADP/NADPH was calculated as a ratio of (total NADP minus NADPH) divided by NADPH.

2.5. Endothelial function

Mesenteric arterioles of 3rd order were isolated from anesthetized mice and placed into ice-cold phosphate-buffered saline (PBS) while excising surrounding connective and adipose tissue. Mesenteric arteriole rings (≈2 mm) were mounted isometrically under a resting force of 1.5 mN in tissue chambers of the M-series myograph system (Radnoti LLC) containing an oxygenated Krebs–Henseleit (K–H) buffer warmed to 37 °C. Rings were allowed to equilibrate for 90 min and maximal contractions to 100 mM KCl were used for normalization. Dose-responses were tested using log-based addition of phenylephrine (3 nM–10 μM). An EC_{50} of phenylephrine was added to contract the rings and dose–response was tested using the endothelial-dependent vasodilator acetylcholine (10 nM–3 μM). Endothelial-independent vasodilation was assessed using sodium nitroprusside (1 nM–100 μM). Rings were rinsed with fresh K–H buffer between each test until they returned to baseline resting tension.

2.6. Leukocytes adhesion

For large vessels, blood was drawn via cardiac puncture and collected into K2-EDTA. As described [21], leukocytes were isolated using a double-density Percoll gradient (500 g, 35 min, room temperature). PMN bands were suspended in serum-free DMEM, and fluorescently labeled using a PKH26GL staining kit, (Sigma–Aldrich). Labeled cells were co-incubated with the isolated thoracic aortic 4 mm-segments (in DMEM-supplemented with 10% fetal bovine serum (FBS) and kept at 4 °C before switching to 37 °C for an hour and leukocytes added). Shear stresses were applied by means of an orbital shaker platform heated to 37 °C for 60 min. Aortic segments were removed and PBS-washed, placed on a glass microscope slide for immersion oil. Leukocytes adhering to the endothelium were observed at 200×-magnification using an epifluorescent microscope. 3–4 fields/aorta were used and findings expressed as total number of cells/microscopic field.

To measure leukocyte adhesion in the microcirculation, quantitative intravital microscopy (IVM) of the mesentery was carried out as described [25]. Four distal loops of ileal tissue, exteriorized through a midline incision laparotomy, were superfused with 37 °C K–H buffer in an intravital microscopy Plexiglas chamber attached on the stage of an Eclipse FN1 Physiostation Microscope (Nikon Corporation). Relatively straight, unbranched segments of post-capillary venules with lengths of >100 μm and diameters between 25 and 40 μm were used. Observation of the mesenteric microcirculation was made with 20× salt water-immersion lens. Images were projected by high-resolution, intensified video cameras (XR-Mega-10 EX ICCD; Stanford Photonics) onto a high-resolution, color video monitor (Multiscan 200-sf, Sony) and the image recorded on a WIN-XP Imaging Workstation. Data were analyzed using computerized imaging software (Micro-Manager). Leukocyte adherence was defined as the number of leukocytes firmly adhered to 100 μm-length of endothelium for at least 30 s.

2.7. Immunofluorescence analysis of aortic roots

Mice were perfused through the left ventricle with 4% (wt/vol) paraformaldehyde as described [26]. Briefly, the aortic root was embedded in OCT medium, frozen and cut in 10 μm-sections onto Fisher Superfrost Plus-coated slides, fixed and incubated with anti-VCAM-1 antibody (Southern Biotech; 1:100) followed by anti-rat Alexa-fluor 555 (Cell Signaling, 1:2000, 1 h). In the negative control, VCAM-1 antibody was replaced by an equivalent dilution of normal rat serum (NRS).

2.8. Echocardiography

Transthoracic echocardiography was performed using an Acuson System equipped with a 15-mHz transducer. Mice were anesthetized with 1–2% isoflurane by inhalation with heart rate (360–500 beats/min) and core temperature (36–37 °C) continuously being monitored. Cardiac geometry and functional parameters [wall thickness and left ventricular cardiac function (ejection fraction and fractional shortening)] were measured from images obtained using two-dimensional B-Mode and M-mode views. Doppler ultrasound of mitral and aortic flow was obtained to determine the myocardial performance index (MPI) (or Tei index), calculated as: (IVRT + IVCT)/ET.

2.9. Heart histology

Hearts were fixed by 10% Formalin, paraffin-embedded and sectioned into 4 μm consecutive sections to be stained by hematoxylin and eosin (H&E). Myocyte size analysis was performed under microscopic examination of H&E stained sections at 20× magnification. The area of each myocyte was assessed and the average area/microscopic field/section were calculated. Images were collected using NIS-Element BR.1 software. Because processing of paraffin-embedded sections alters the original tissue thickness and causes shrinkage, we performed simultaneous processing of the sections from all mouse groups to be able to carry out relative comparisons of myocyte areas in the specimens examined in these studies.

2.10. Primary cardiac cells

Cardiac myocytes were isolated from 2 to 3 months old mice as described [27]. Briefly, mice were anesthetized with an intraperitoneal injection of pentobarbital as above. The descending aorta was cut and the heart was immediately flushed by injecting the right ventricle with 7 ml of 5 mmol/l EDTA-supplemented perfusion buffer (130 mmol/l NaCl, 5 mmol/l KCl, 0.5 mmol/l NaH_2PO_4, 10 mmol/l HEPES, 10 mmol/l Glucose, 10 mmol/l2,3-butanedione monoxime (BDM), 10 mmol/l Taurine). Following clamping the ascending aorta, the heart was removed and transferred to a 60 mm-dish before the left ventricle was sequentially perfused with 10 ml of EDTA-supplemented perfusion buffer, followed by 3 ml of 1 mmol/l $MgCl_2$-supplemented perfusion buffer, and 30–50 ml of collagenase buffer [collagenase type II and type IV (0.5 mg/ml) (Worthington) in $MgCl_2$-perfusion buffer]. Following assessment of myocyte yield and percentage of viable rod-shaped cells using a hemocytometer, the cell pellet containing myocytes was resuspended in pre-warmed plating media M199 (Gibco) supplemented with 5% fetal bovine serum (FBS), 10 mmol/l BDM (Sigma Aldrich), and 1% Penicillin–Streptomycin (Gibco), and plated on a laminin (5 μg/ml) pre-coated 6-well tissue culture plates and placed in a humidified tissue culture incubator (37 °C, 5% CO_2) for 1 h. Media was then replaced with fresh, pre-warmed culture media (M199 Gibco), supplemented with 0.1% BSA (Sigma Aldrich), BDM (10 mmol/l), and 1% Penicillin Streptomycin for 24 h before myocytes were collected and analyzed.

Cardiac endothelial cells were isolated from 2-month-old mice using 2 mg/ml Collagenase A (Roche) dissolved in Dulbecco's Phosphate Buffered Saline containing $CaCl_2$ and $MgCl_2$ (Gibco), as described [28]. Cells were sorted by binding to anti-mouse CD31 Dynabeads immobilized on the tube wall using Magnetic Particle Concentrator DynaMag™-15. Immuno-selected CD31-positive cells were resuspended in 8 ml growth medium [DMEM (Gibco) containing 0.01% heparin and 10% Bovine Endothelial Cell Growth Supplement-ECGS (Cell Applications), 20% FBS and 1% Penicillin–Streptomycin] and plated on a 10 cm plate coated with 0.1% gelatin in a humidified tissue culture incubator (37 °C, 5% CO_2). Thereafter, Growth medium was replaced every other day until cells reached ~80% confluency at which point, they were trypsinized and incubated with rat anti-mouse CD102-coupled Dynabeads (Invitrogen) and immobilized on the tube wall as above, washed, resuspended, and plated in 10 cm gelatin-coated plates.

2.11. Western blot analysis

Western blot analysis was performed using 1:1000 of the following polyclonal antibodies from Cell Signaling (Danvers, MA) against: phospho-Akt (Ser 473), Akt, phospho-p44/42 MAPK (Thr 202/Tyr204), p44/42 MAPK, phospho-eNOS (Ser1177), eNOS, phospho-Foxo1 (Ser256), Foxo1, phospho-IRS1 (Ser612), IRS1, Shc, and VCAM-1. We also used antibodies against phospho-insulin receptor beta subunit (pIRβ) (phospho-Y1361), IRβ (Abcam, Cambridge, MA); and cleaved Caspase 3 (EDM Milipore, Billerica, MA). As previously shown [19], we used custom-made rabbit polyclonal antibodies Ab 3759 against the mouse CEACAM1 extracellular domain, the rat CEACAM1 (αP3[Y488]) and phospho-CEACAM1 (α-pCC1) mouse antibodies

(Bethyl Laboratories, Montgomery, TX). For normalization, α/β-tubulin antibody (Cell Signaling) was used at 1:5000 dilution. Blots were incubated with horseradish peroxidase-conjugated sheep anti-mouse IgG or donkey anti-rabbit IgG antibody (GE Healthcare Life Sciences, Amersham, Sunnyvale, CA) and subjected to enhanced chemiluminescence (ECL, Amersham Pharmacia).

For co-immunoprecipitation experiments, polyclonal antibodies against Shc (B-9) (Santa Cruz Biotechnology, Dallas, TX) and IRS1 (Cell signaling) were used to immunoprecipitate proteins from tissue lysates. To avoid detection of the antibody heavy chain, membranes were incubated with horseradish peroxidase-conjugated IgG fraction monoclonal mouse anti-rabbit IgG, light chain specific (Cat # 211-032-171, Jackson Immuno-Research laboratories).

2.12. Quantitative real time-PCR

cDNA was synthesized using Superscript III (Bio-Rad), and qRT-PCR was performed using Fast SYBR Green Master Mix by the ABI StepOnePlus Real-Time PCR System (Applied Biosystems), as described [23]. Primers were used at a final concentration of 10 μM (Table S1) and mRNA was normalized to 18S.

2.13. Statistical analysis

Parametric data were analyzed by one-way analysis of variance (ANOVA) with Tukey's test for multiple comparisons. Nonparametric data were analyzed by Kruskal–Wallis test with Dunn's correction for multiple pairwise comparisons. Statistical analysis was performed using GraphPad Prism-6 software.

3. RESULTS

3.1. Hepatic-specific rescuing of CEACAM1

qRT-PCR analysis detected mouse mRNA (m*Cc1*) in the heart, as well as the cardiac endothelial cells and myocytes of wild-type $Cc1^{+/+}$, but not $Cc1^{-/-}$ or $Cc1^{-/-xliver+}$ mice (Table S2). Rat mRNA (r*Cc1*) expression was restricted to the liver of $Cc1^{-/-xliver}$ mice (Table S2), as previously shown [19]. Consistently, Western blot analysis detected endogenous mouse CEACAM1 (mCC1) in the liver of $Cc1^{+/+}$, but not $Cc1^{-/-}$ or $Cc1^{-/-xliver+}$ mice (Figure 1A). In contrast, immunoblotting with rat CEACAM1 antibody (Ib: α-rCC1) revealed transgenic rat CEACAM1 expression in the liver of $Cc1^{-/-xliver+}$ (Figure 1A). As previously shown [19], rat CEACAM1 protein was not detected in extra-hepatic tissues of $Cc1^{-/-xliver+}$ mice, including the heart and aorta (Figure 1A).

3.2. $Cc1^{-/-}$, but not $Cc1^{-/-xliver+}$ mice, exhibit abnormal endothelium-dependent relaxation

$Cc1^{-/-}$ mice continues to exhibit chronic hyperinsulinemia at 8 months of age (Figure 1B*i*) resulting from impaired insulin clearance (steady-state C-peptide/insulin molar ratio) (Figure 1B*ii*). Hyperinsulinemia caused insulin resistance, as demonstrated by hyperinsulinemic-euglycemic clamp analysis [15,19], and elevated plasma non-esterified fatty acids (NEFA) (Figure 1B*iii*). As recently reported [19], these metabolic abnormalities were all reversed by rescuing CEACAM1 exclusively in the liver of $Cc1^{-/-xliver+}$ mice (Figure 1B).

$Cc1^{-/-}$ manifested elevated systolic blood pressure and kidney dysfunction starting at 6 months of age in association with increased intrarenal RAS activity [22]. Consistent with hemodynamic changes associated with elevated RAS activity, $Cc1^{-/-}$ mice manifested albuminurea (Figure 2A*i*) and a higher albumin-to-creatinine ratio (UACR) (Figure 2A*ii*), which was reversed by liver-specific rescuing of *Ceacam1*.

Because elevated RAS is also associated with endothelial dysfunction [29], we next examined the %vasorelaxation in rings from mesenteric arterioles or vessel function with 100 mM KCl and log-based additions of acetylcholine (Ach) (Figure 2B*ii*) and sodium nitroprusside (SNP) (Figure 2B*iii*) normalized to maximum contraction in response to phenylephrine (PE) (Figure 2B*i*). Unlike the insignificant effect of nitroprusside (Figure 2B*iii*), the Emax of endothelial-dependent vasodilation of phenylephrine-precontracted rings in response to acetylcholine was increased in $Cc1^{-/-}$ relative to $Cc1^{+/+}$ mice (Figure 2B*ii*). This was prevented in $Cc1^{-/-xliver+}$ transgenics (Figure 2B*ii*). Thus, endothelial-dependent vasodilation was impaired in $Cc1^{-/-}$ in association with the loss of CEACAM1 in liver. Consistent with reduced NO bioavailability in association with impaired vasodilation in response to acetylcholine [6], basal plasma NO levels were lower in $Cc1^{-/-}$ than $Cc1^{+/+}$ wild-types (Figure 2C), as previously shown [21]. This was accompanied by a reciprocal increase in plasma endothelin-1 (ET-1) levels (Figure 2D), which could in part stem from lower plasma PGE2 levels (Figure 1B*iv*), as reported [30,31]. Liver-specific CEACAM1 rescuing restored plasma NO and ET-1 levels (Figure 2C–D; $Cc1^{-/-xliver+}$ versus $Cc1^{-/-}$ mice).

3.3. $Cc1^{-/-}$, but not $Cc1^{-/-xliver+}$ mice, exhibit an increase in inflammation and leukocyte adhesion

Because in addition to low NO bioavailability, inflammation and leukocyte-endothelium adhesion increase in the early phase of endothelial dysfunction [6], we further investigated the implication of *Ceacam1* deletion in endothelial function by carrying out intravital microscopy to measure leukocyte adhesion. As shown in Figure 3A*i*, the venular endothelium of $Cc1^{-/-}$ displayed an increase in adhesiveness to circulating leukocytes, as evidenced by the ~2.5-fold increase in leukocyte adhesion in mesenteric post-capillaries. This was curbed by restoring CEACAM1 expression in liver.

Parallel *ex-vivo* experiments with leukocytes isolated from $Cc1^{-/-}$ aortae demonstrated a significantly higher (~3.5-fold) pro-adhesive phenotype compared with wild-type controls (Figure 3A*ii*), as previously reported [21]. Restoring CEACAM1 expression in liver normalized this phenotype in $Cc1^{-/-xliver+}$ mice, bringing the number of adhering leukocytes to levels comparable to that in control mice.

Consistent with increased adhesion of leukocytes both in microcirculation and large conduit arteries in $Cc1^{-/-}$ mice, the mRNA (Table S3) and protein levels of VCAM-1, a critical mediator of leukocytes recruitment to the endothelium [32,33], was higher in $Cc1^{-/-}$ than $Cc1^{+/+}$ aortae, as shown by Western blot (Figure 3B) and immunofluorescence analysis of aortic root sections (Figure 3C*ii–ii'* versus C*i*). Liver-specific rescuing of CEACAM1 restored normal aortic *Vcam-1* mRNA (Table S3) and VCAM-1 protein levels (Figures 3B and C*iii*). Similarly, the mRNA levels of other cell adhesion molecules such as *Icam-1* and *P-selectin* were ~2-fold higher in $Cc1^{-/-}$ than $Cc1^{+/+}$ and $Cc1^{-/-xliver+}$ mice (Table S3).

Plasma IL-6 and TNFα levels were elevated in $Cc1^{-/-}$ relative to $Cc1^{+/+}$ and $Cc1^{-/-xliver+}$ mice (Figure 1B*v* and B*vi*, respectively). Similarly, the mRNA levels of macrophage markers (*F4/80 and Cd68*) and TNFα were higher in the aortae of $Cc1^{-/-}$ than $Cc1^{+/+}$ and $Cc1^{-/-xliver+}$ mice (Table S3). Consistent with increased TNFα infiltration in association with aortic lipid accumulation in vascular disease [34], the mRNA levels of the fatty acid transporter *Cd36* and fatty acid synthase (*Fasn*) were elevated in $Cc1^{-/-}$ aortae (Table S3), as predicted from hyperinsulinemia-driven activation of lipogenic gene expression [17]. In support of enhanced oxidative stress by TNFα, $Cc1^{-/-}$ aortae manifested lower basal aortic NO levels (Figure 2E) and higher mRNA levels of oxidative stress genes (*Nox1*, *Nox4* and *gp91*) than their $Cc1^{+/+}$ counterparts (Table S3). These

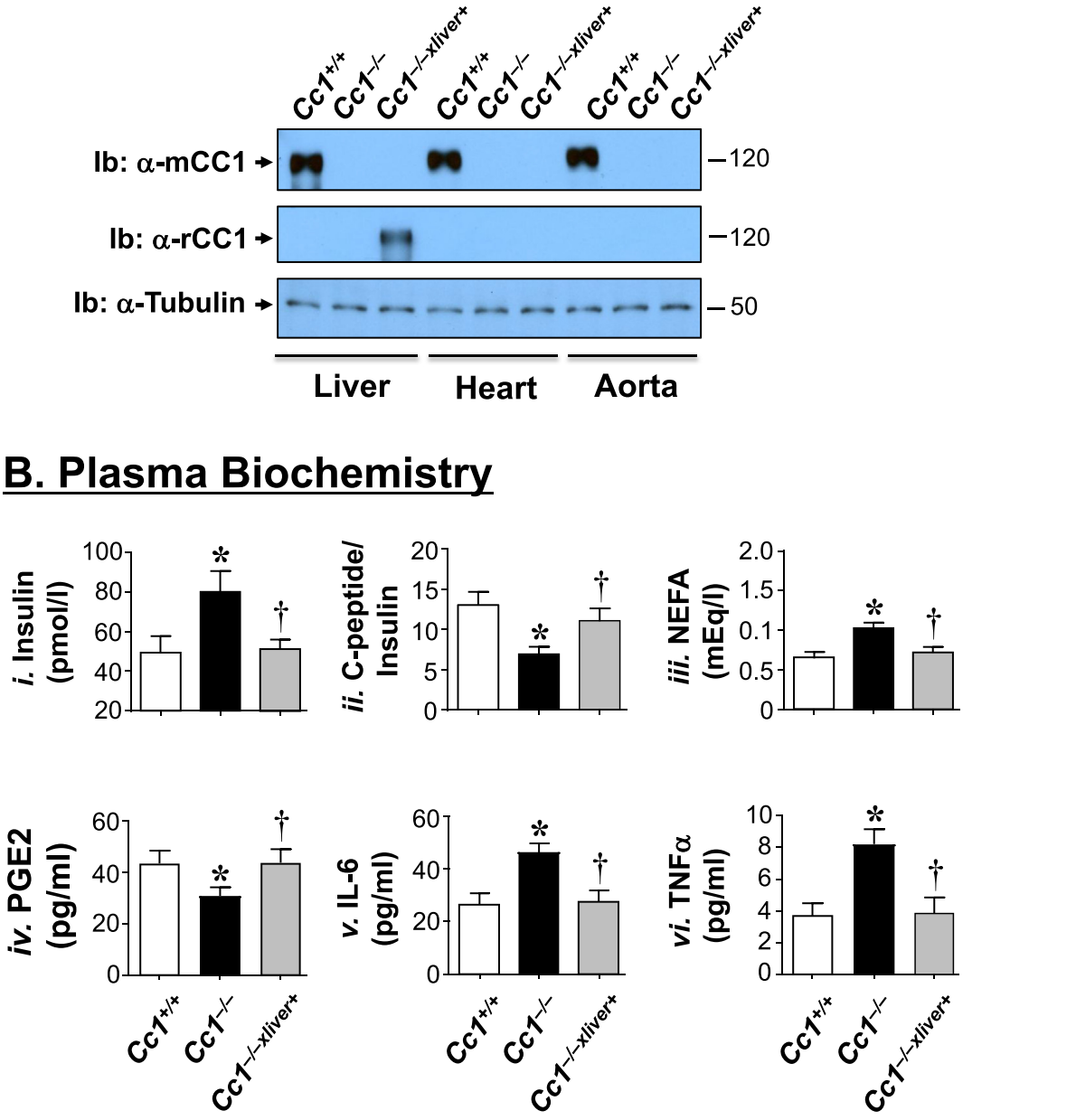

Figure 1: Metabolic phenotype. (A) Protein levels of mouse (mCC1) and rat CEACAM1 (rCC1) were analyzed by immunoblotting (Ib) with either a polyclonal antibody against mouse (upper gel), or rat CEACAM1 (middle gel). The lower part of the blot was immunoblotted with an antibody against Tubulin to normalize for protein loading. The apparent molecular weight (kDa) is indicated at the right hand-side of each gel. Gels represent more than two separate experiments performed on different mice per group. (B) Retro-orbital blood was drawn from $Cc1^{+/+}$ (white), $Cc1^{-/-}$ (black) and $Cc1^{-/-xliver+}$(gray) mice (n $\geq$ 5 mice/genotype; 7-to-8 months of age) to assess plasma insulin (*i*), steady-state C-peptide/insulin molar ratio as measure of insulin clearance (*ii*), non-esterified fatty acids (NEFA) (*iii*), PGE2 (*iv*), IL-6 (*v*) and TNFα (*vi*). Assays were performed in triplicate. Values are expressed as mean $\pm$ SEM. *$P \leq 0.05$ versus $Cc1^{+/+}$, †$P \leq 0.05$ $Cc1^{-/-xliver+}$ versus $Cc1^{-/-}$.

parameters were all normalized in $Cc1^{-/-xliver+}$ mice (Figure 2E and Table S3).

3.4. $Cc1^{-/-}$ mice manifest blunted aortic insulin signaling

Because altered insulin action reduces NO bioavailability and elevates ET-1 levels to tip the balance towards reducing vasodilation [2,4], we then examined insulin signaling in aortic lysates. To this end, mice were subjected to an overnight fast (F) prior to refeeding for 7 h to release insulin (Figure 4A). As expected from chronic hyperinsulinemia [35], immunoblotting (Ib) with an antibody against the beta subunit of the insulin receptor (α-IRβ) and against tubulin (α-tubulin) to normalize against total protein loaded showed a 50% decrease in the insulin receptor protein level in the aorta of $Cc1^{-/-}$ relative to $Cc1^{+/+}$ mice (Figure 4B middle gel against lower gel), as we have shown in the liver and hypothalamus [19]. This reduced IRβ phosphorylation, as immunoblotting with α-phospho-IRβ antibody revealed (Figure 4B, top gel).

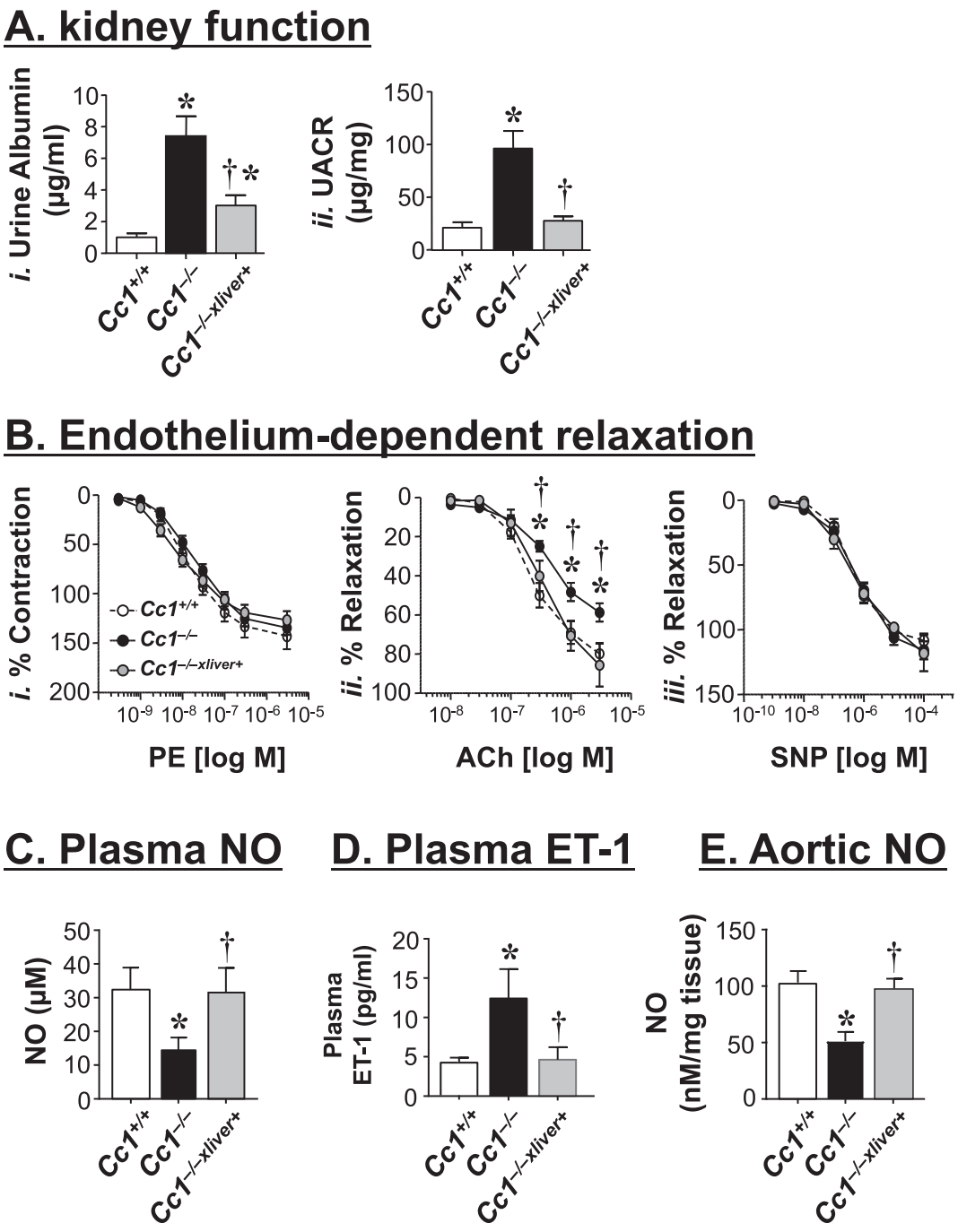

Figure 2: Endothelium-dependent relaxation in mesenteric arterioles. (A) Urine albumin levels (*i*) and urine albumin-to-creatinine ratio (UACR) (*ii*) were determined in 6 month-old $Cc1^{+/+}$ (white), $Cc1^{-/-}$ (black) and $Cc1^{-/-xliver+}$ mice (gray) (n = 6–7/genotype). Values are expressed as mean ± SEM. (B) Nitric oxide (NO) release was determined in phenylephrine (PE)-pre-contracted arterioles (*i*), following stimulation with acetylcholine (Ach) (*ii*) and sodium nitroprusside (SNP) (*iii*) from 8 to 9 month-old mice (n = 5–6/genotype). Values are expressed as mean ± SEM. $*P \leq 0.05$ versus $Cc1^{+/+}$ and $\dagger P \leq 0.05$ versus $Cc1^{-/-}$. (C) Plasma NO, (D) plasma endothelin-1 (Et-1) and (E) aortic NO levels were assayed in triplicate in n ≥ 5 mice/genotype (7-to-8 months of age). Values are expressed as mean ± SEM. In A–E, $*P \leq 0.05$ versus $Cc1^{+/+}$, $\dagger P \leq 0.05$ $Cc1^{-/-xliver+}$ versus $Cc1^{-/-}$.

It also reduced the phosphorylation of downstream signaling molecules such as IRS1, Akt, eNOS, and Foxo1 (Figure 4C–F). Rescuing CEACAM1 in the liver reversed basal hyperinsulinemia (Figure 4A) and subsequently, the level and phosphorylation of IRβ (Figure 4B) and of its downstream signaling molecules (Figure 4C–F). Together, this indicates that hyperinsulinemia contributed to dysregulated insulin-dependent activation of eNOS, and subsequently, lower NO production in $Cc1^{-/-}$ aortae.

In contrast, insulin induced MAPKinase phosphorylation to a larger extent in $Cc1^{-/-}$ than $Cc1^{+/+}$ and $Cc1^{-/-xliver+}$ aortae (Figure 4G), in parallel to a higher binding of Shc to IRβ in aortic lysates of the hyperinsulinemic $Cc1^{-/-}$ by comparison to its normo-insulinemic

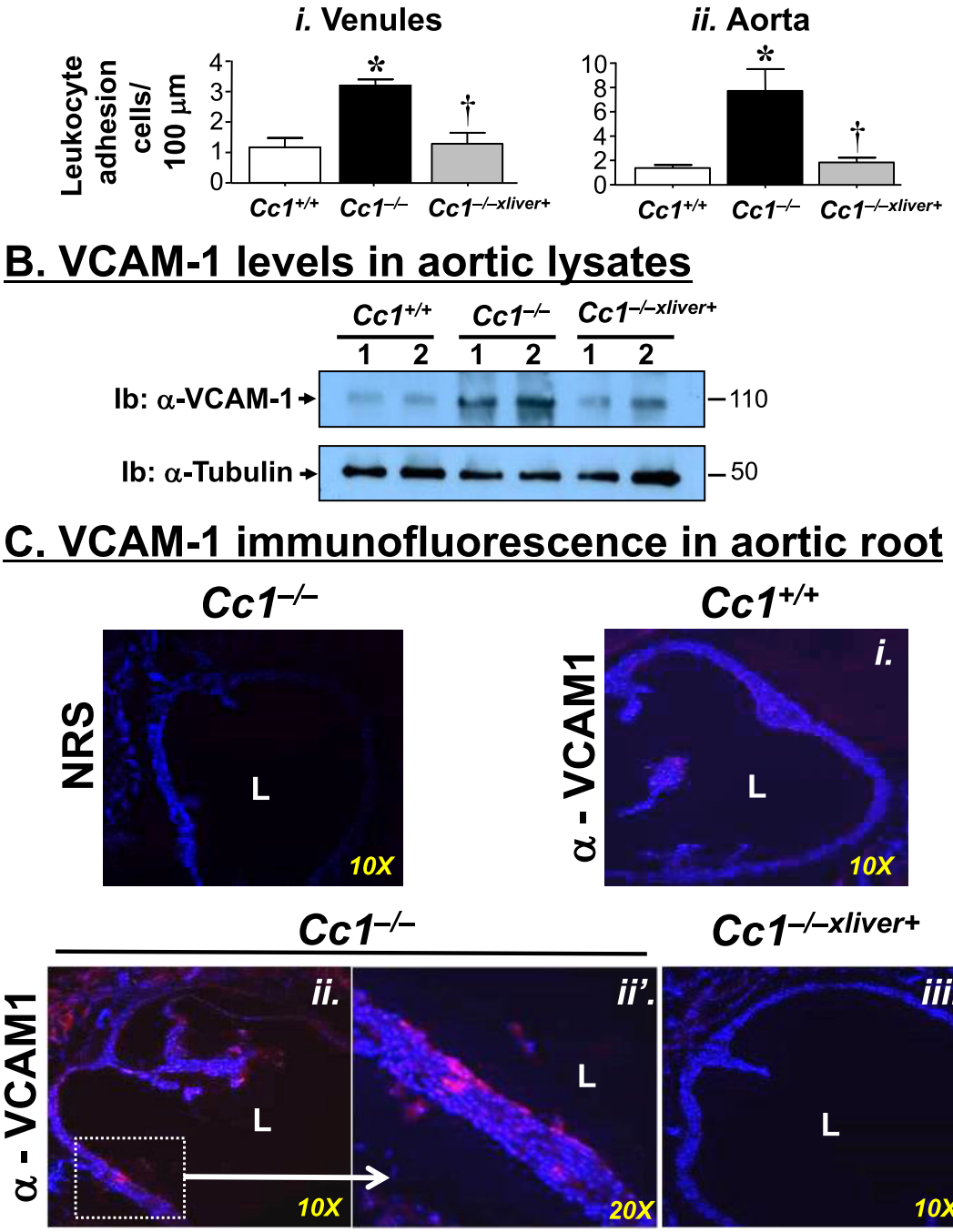

Figure 3: Leukocyte-endothelium adhesion in aorta. (A) Mesenteric venules (*i*) and aortae (*ii*) of 8–9 month-old $Cc1^{+/+}$ (white bar), $Cc1^{-/-}$ (black bar) and $Cc1^{-/-xliver+}$ mice (gray bar) (n = 5–7/genotype) were removed and their leukocytes–endothelium interaction was assayed. Values are expressed as mean ± SEM. $*P \leq 0.05$ versus $Cc1^{+/+}$ and $\dagger P \leq 0.05$ $Cc1^{-/-xliver+}$ versus $Cc1^{-/-}$ mice. (B) Western blot analysis of lysates from aorta of 8-month-old mice using α-VCAM-1 antibody to immunoblot (Ib) the upper half and α-tubulin to immunoblot the lower half for normalization against the amount of total proteins loaded. The apparent molecular weight (kDa) is indicated at the right hand-side of each gel. Gels represent more than two separate experiments performed on different mice per group. (C) Immunofluorescence analysis of VCAM-1 expression in the aortic root of 9 month-old mice (n = 5/genotype). DAPI blue staining was used to detect nuclei and visualize tissue context. Red VCAM-1 staining was higher in sections from $Cc1^{-/-}$ mice (both *ii* at 10× and *ii'* in the enlarged field at 20×) versus $Cc1^{+/+}$ (*i*) and $Cc1^{-/-xliver+}$ (*iii*). To control for VCAM-1 antibody specificity, some $Cc1^{-/-}$ sections were incubated with normal rat serum (NRS) as a non-specific primary antibody. L: The luminal aspect of the vessels was included for reference.

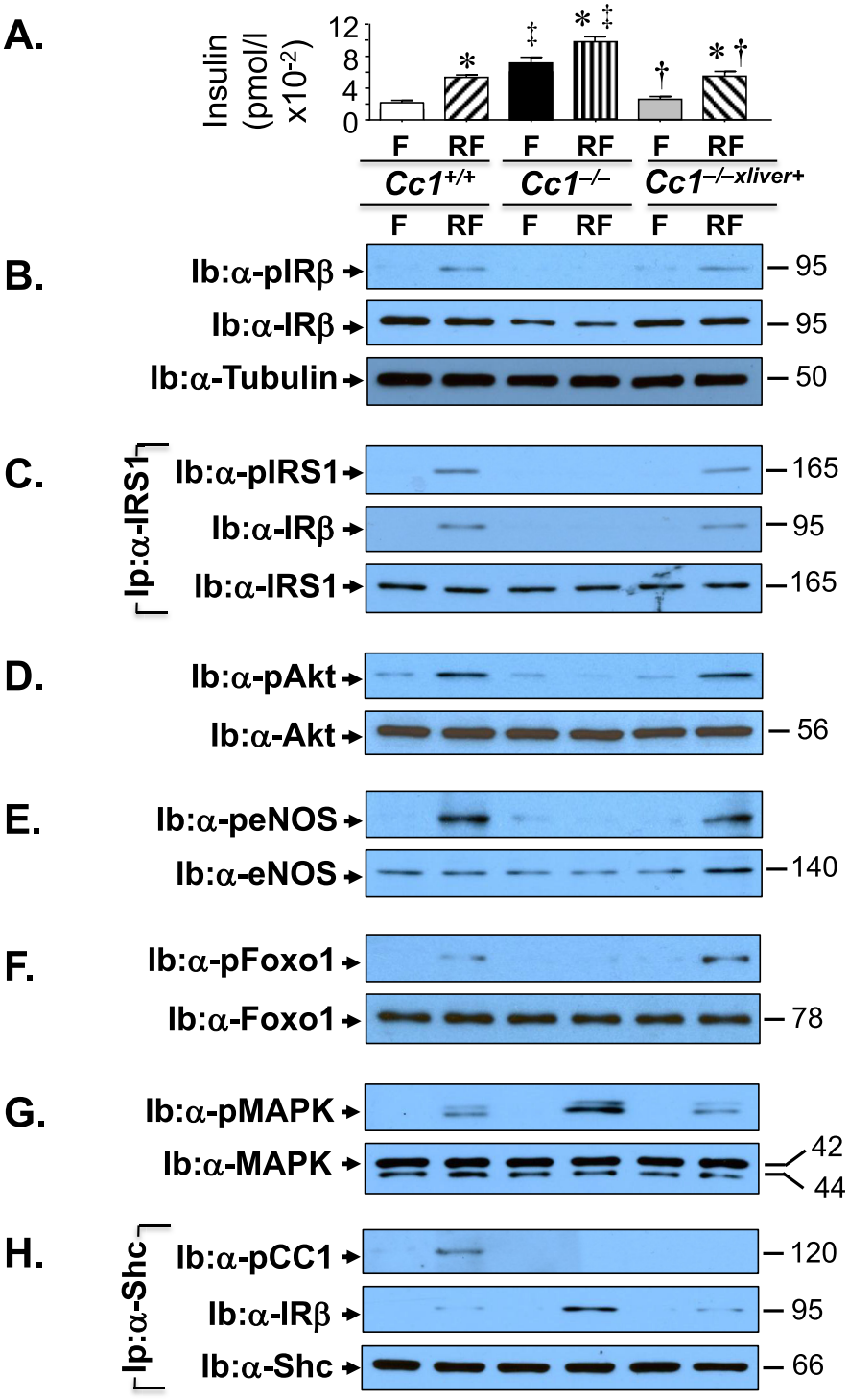

Figure 4: Insulin signaling in aorta. (A) Mice (8 months of age, n = 6/genotype/treatment) were fasted (F) overnight and refed for 7 h (RF) before retro-orbital venous blood was drawn and plasma insulin levels were assayed, as indicated in the graph [$Cc1^{+/+}$ (white for F and right diagonal stripes for RF), $Cc1^{-/-}$ (black for F and vertical stripes for RF), and $Cc1^{-/-xliver+}$ (gray for F and left diagonal stripes for RF)]. Values are expressed as mean ± SEM. $*P \leq 0.05$ versus $Cc1^{+/+}$, $\dagger P \leq 0.05$ $Cc1^{-/-xliver+}$ versus $Cc1^{-/-}$ mice/treatment group and $\ddagger P \leq 0.05$ $Cc1^{-/-}$ versus others/treatment group. (B) Western analysis of lysates from aortae was performed to assess insulin receptor protein level (Ib: α-IRβ) and phosphorylation (Ib: α-pIRβ). The lower half of the gel was used to immunoblot with α-Tubulin antibody for protein normalization. (D–G) Lysates were subjected to Western blot analysis using antibodies against phosphorylated (p) Akt (D), eNOS (E), Foxo1 (F) and MAPkinase (G) (top gels), and with antibodies against the proteins to control for loading (lower gels). (B) Some aliquots were subjected to immunoprecipitation (Ip) with α-IRS1 antibody followed by immunoblotting with antibodies against phosphor-IRS1 (pIRS1, top gel), IRβ (middle gel), or IRS1 (bottom gel). (H) Other aortic lysates were subjected to immunoprecipitation (Ip) with α-Shc antibody followed by immunoblotting (Ib) with antibodies against phospho-CEACAM1 (pCC1, top gel), IRβ (middle gel) or Shc (lower gel). The apparent molecular weight (kDa) is indicated at the right hand-side of each gel. Gels represent 2 separate experiments performed on different mice/genotype/treatment.

counterparts, as shown by the higher level of IRβ detected by immunoblotting the Shc immunopellet (Ip) with α-IRβ antibody (Figure 4H, middle gel). This occurred in parallel to the reciprocal decrease in IRS1 binding to IRβ, as shown by immunoblotting the IRS1 immunopellet with α-IRβ antibody (Figure 4B, middle gel). Because Shc competes with IRS1 for NPEY960 in the juxtamembrane domain of the insulin receptor [36], it is conceivable that lower IRS1 phosphorylation and binding to IRβ gave way to more Shc binding to IRβ in $Cc1^{-/-}$ aortae, which in turn led to more coupling of the Ras/MAP-kinase pathway to the receptor, and its superior activation in $Cc1^{-/-}$ relative to $Cc1^{+/+}$ and $Cc1^{-/-\text{xliver}+}$ aortae. This could contribute to the higher mRNA levels of ET-1 *(Et-1)* [2,4] and its -A and -B receptors in the aortae of $Cc1^{-/-}$ mice as compared to the other mouse groups (Table S3. *Etar* and *Etbr*). Consistent with the lower vasodilation tone, the ratio of *Etar*/*Etbr* was ~5-fold higher in the aortae of $Cc1^{-/-}$ as compared to the other mouse groups (Table S3).

3.5. $Cc1^{-/-}$ mice manifest altered cardiac performance and myocardial hypertrophy

Obesity and hypertension are associated with left ventricular hypertrophy [37,38]. Thus, we next performed transthoracic cardiac ultrasound to assess cardiac structure and function in 6 month-old male mice. Echocardiography demonstrated increased septal wall thickness (SWTd) (Figure 5A*i*) and posterior wall thickness (PWTd) (Figure 5A*ii*) in $Cc1^{-/-}$, but not $Cc1^{-/-\text{xliver}+}$ mice. Moreover, the relative wall thickness was also elevated in null mutants, but not in $Cc1^{-/-\text{xliver}+}$

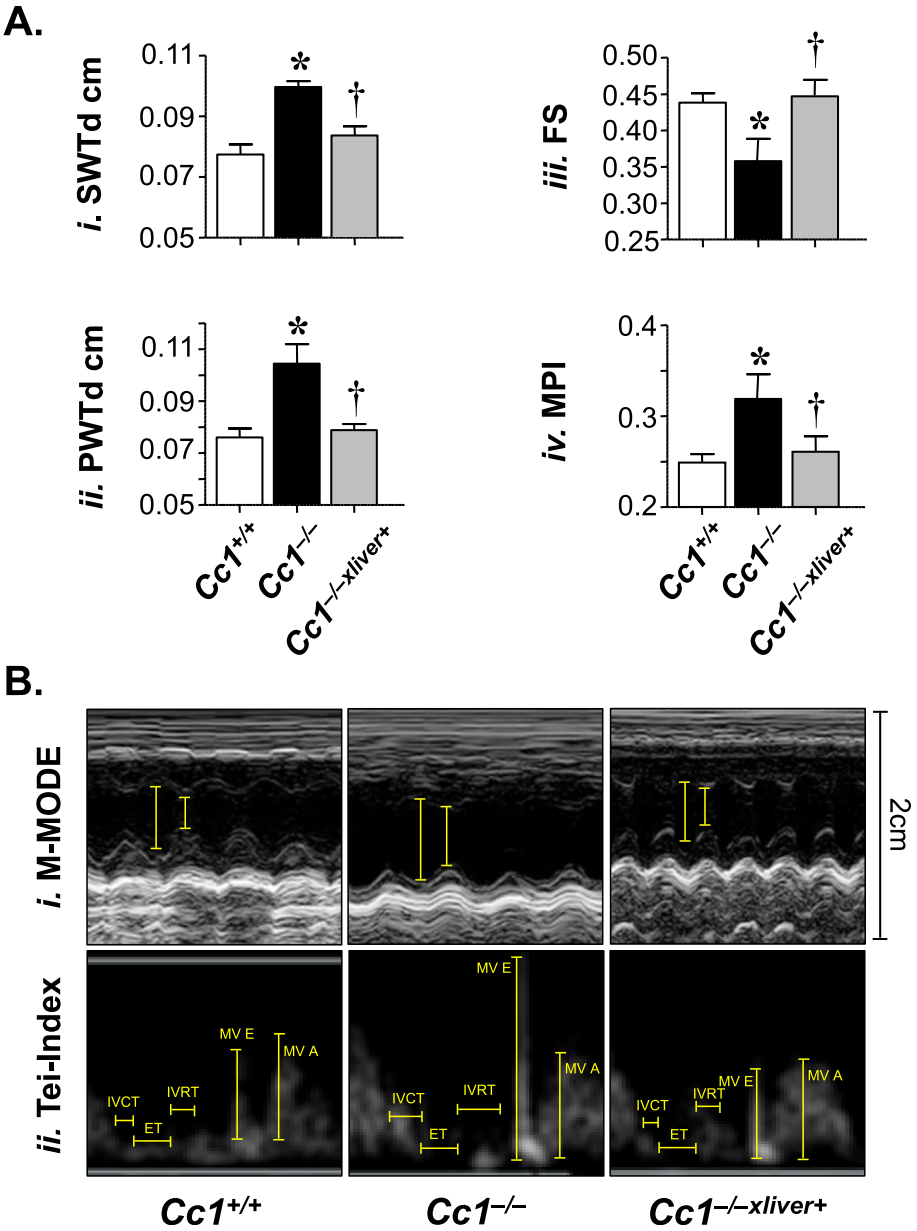

Figure 5: Echocardiography analysis. (A) Representative echocardiography analysis in 6 month-old $Cc1^{+/+}$ (white bar), $Cc1^{-/-}$ (black bar) and $Cc1^{-/-xliver+}$ mice (gray bar) (n = 10/genotype). Septal wall thickness at end diastole (SWTd) (*i*), posterior wall thickness at end diastole (PWTd) (*ii*), fractional shortening (FS) (*iii*), myocardial performance index (MPI) (*iv*) were determined. Values are expressed as mean ± SEM. *$P \leq 0.05$ versus $Cc1^{+/+}$ and †$P \leq 0.05$ $Cc1^{-/-xliver+}$ versus $Cc1^{-/-}$ mice. (B) (*i*) Representative M-mode of each mouse type demonstrating cardiac hypertrophy and reduced wall motion of $Cc1^{-/-}$ mice. $Cc1^{-/-xliver+}$ mice manifest normal LV geometry and function.

mice (Table S4). Together, this suggested left ventricular hypertrophy in $Cc1^{-/-}$ mice, as further shown by the M-mode representation of the heart (Figure 5B*i*). Cardiac hypertrophy in $Cc1^{-/-}$ by comparison to $Cc1^{+/+}$ and $Cc1^{-/-\text{xliver}+}$ mice was confirmed by the higher heart weight/tibial length ratio (Figure 6A) and the elevation in the mRNA levels of cardiac-hypertrophy markers [Atrial natriuretic factor (Anp); β-myosin heavy chain (β-Mhc) and Brain natriuretic peptide (*Bnp*)] (Figure 6B*i—iii*), in $Cc1^{-/-}$ mice with reversal of these features in $Cc1^{-/-xliver+}$ mice. Consistently, histological examination of H&E-stained myocardial sections (Figure 6C) further revealed a significantly

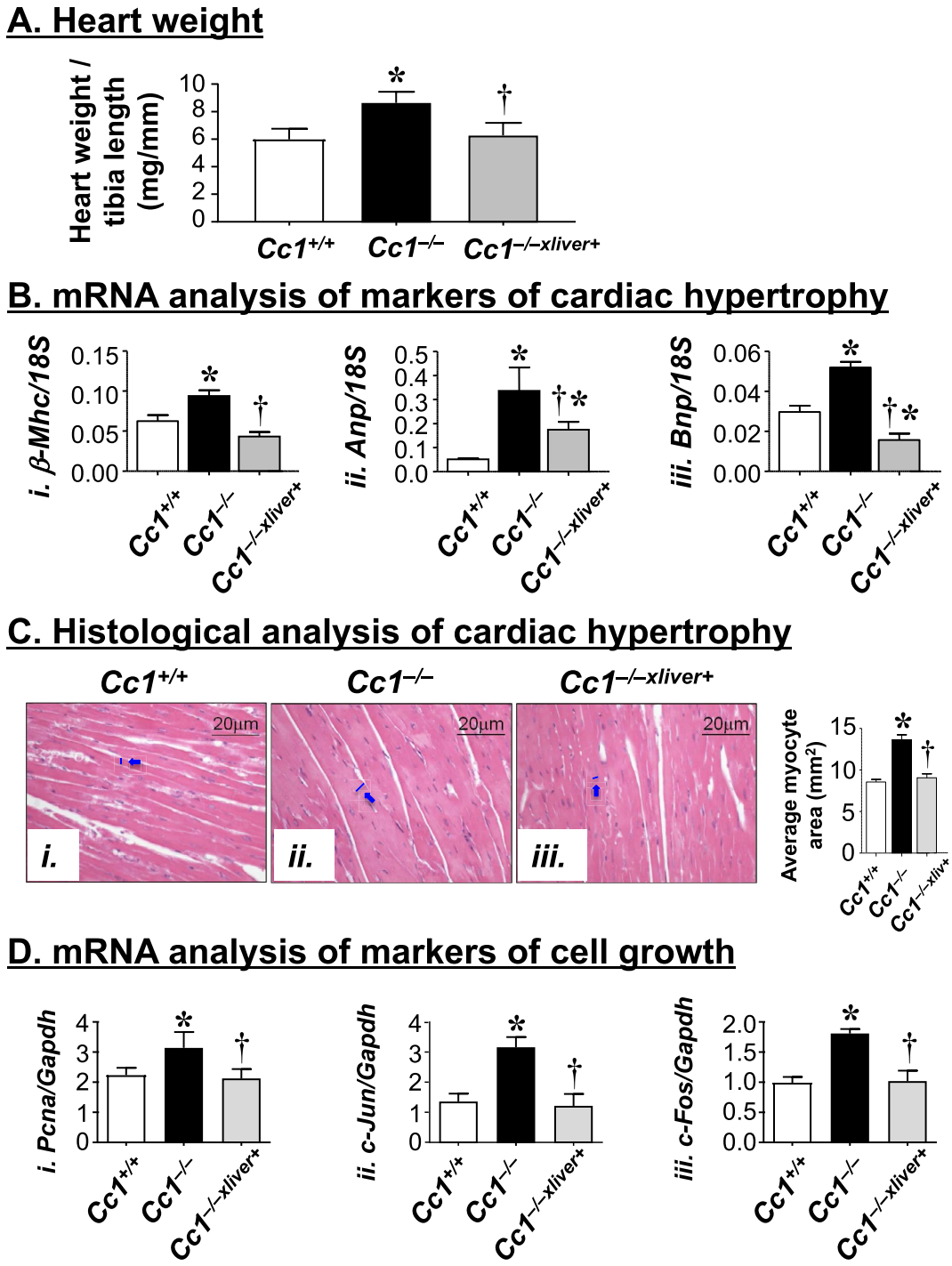

Figure 6: Cardiac hypertrophy analysis. (A) Hearts were removed from male mice (6 month-old, n = 5/genotype), and their weight was normalized to tibial length as a measure of cardiac hypertrophy. (B) qRT-PCR analysis of mRNA of markers of hypertrophy in heart homogenates. These include β-*Mhc* (*i*), *Anp* (*ii*) and *Bnp* (*iii*) (n = 5/genotype in triplicate). (C) H&E stain of heart sections from mice (3 sections/mouse). In the accompanying graph, the average myocyte area was quantitated under the microscope at 20× magnification. (D) mRNA analysis of markers of cell proliferation in heart homogenates. These include *Pcna* (*i*), *c-Jun* (*ii*), and *c-Fos* (*iii*). Analysis was performed relative to *Gapdh* and expressed as mean ± SEM (n = 5/genotype in triplicate). In (A, B and D), values are expressed as mean ± SEM. *$P \leq 0.05$ versus $Cc1^{+/+}$ and †$P \leq 0.05$ $Cc1^{-/-xliver+}$ versus $Cc1^{-/-}$ mice.

enlarged myocyte area in $Cc1^{-/-}$ as compared to that of $Cc1^{+/+}$ hearts (Figure 6C*ii* versus C*i* and accompanying graph). At least in part, this could result from increased cardiomyocyte proliferation, as demonstrated by elevated mRNA levels of markers of cell growth (*Pcna*, *c-Jun* and *c-Fos*) (Figure 6D) in heart lysates. Restoring CEACAM1 expression in liver prevented myocardial hypertrophy (Figure 6C*iii versus* C*i* and accompanying graph) and cardiac cell proliferation (Figure 6D) in null mutants.

Additionally, $Cc1^{-/-}$ mice exhibited decreased left ventricular systolic function, as determined by reduced fractional shortening (FS) (Figure 5A*iii*), fractional shortening area (FSA), and cardiac index (Table S4). In addition, the myocardial performance (MPI), which incorporates measures of both systolic and diastolic function, was elevated in $Cc1^{-/-}$ mice (Figure 5A*iv*). Restoring CEACAM1 expression in the liver fully curbed these cardiac performance measures.

3.6. $Cc1^{-/-}$ mice manifest fat accumulation and oxidative stress in the heart

Because ectopic fat accumulation [39] and oxidative stress [40] cause cardiomyopathy, we then assessed these parameters in the heart. $Cc1^{-/-}$ mice manifested elevated cardiac triacylglycerol levels relative to wild-types (Figure 7A), which was reversed in $Cc1^{-/-xliver+}$ mice. This occurred in parallel to increased mRNA levels of genes involved in fatty acid transport (*Cd36*) and lipogenesis (*Fasn*) (Table S5). *Fasn* mRNA level was also elevated in cardiac endothelial cells (not shown), likely resulting from activated transcription under hyperinsulinemic conditions [17]. Consistently, FASN activity was higher in the null as compared to $Cc1^{+/+}$ and $Cc1^{-/-xliver+}$ mice (Figure 7B).

The content of NO was reduced in the heart of $Cc1^{-/-}$ mice (Figure 7C*i*), in parallel to an increase in oxidative stress (assessed by a rise in NADH/NADPH (Figure 7C*ii*)) and in the mRNA levels of *Nox1*,

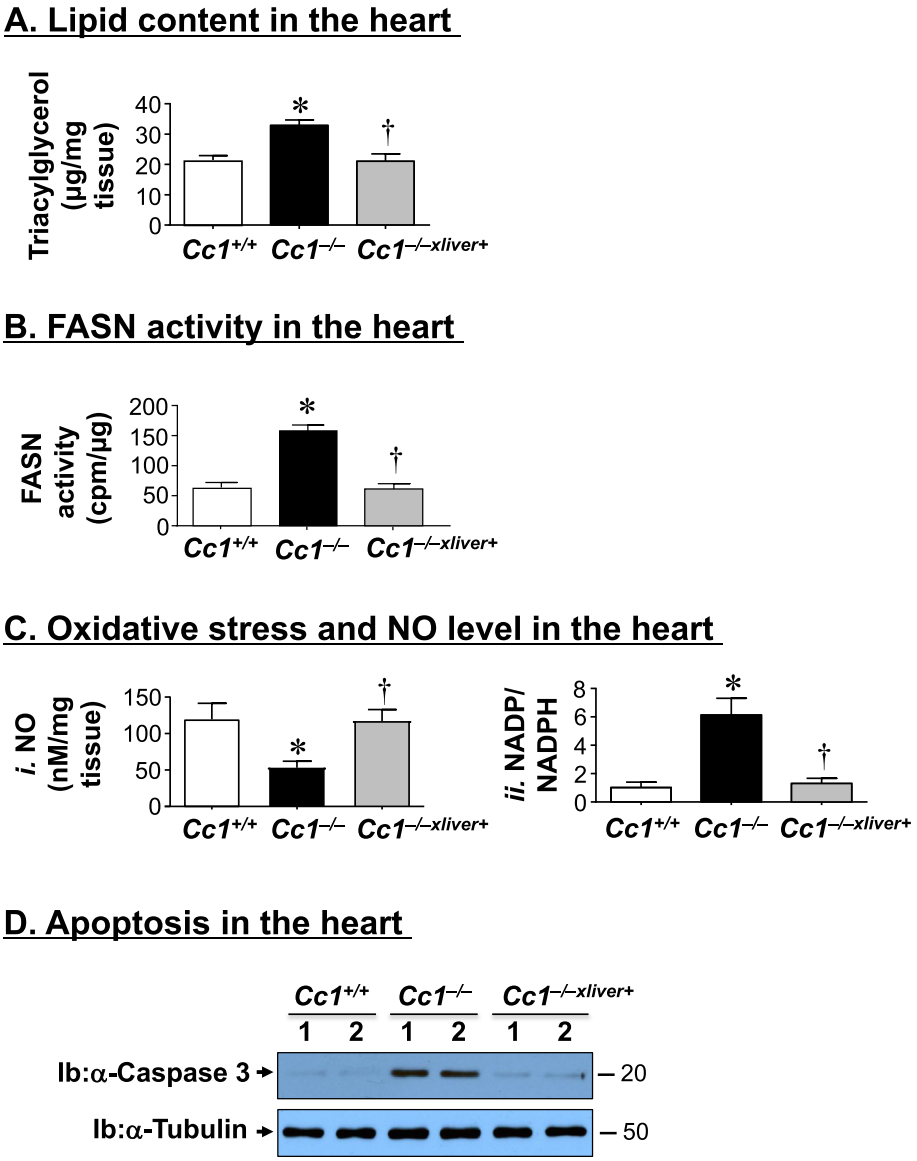

Figure 7: Lipid content, oxidative stress and apoptosis in the heart. The hearts of 6 month-old mice (n = 5/genotype) were assayed in triplicate for (A) triacylglycerol level; (B) fatty acid synthase (FASN) activity by [^{14}C]-malonyl-CoA incorporation; (C*i*) NO content and (C*ii*) NADP/NADPH as measure of oxidative stress. *$P \leq 0.05$ versus $Cc1^{+/+}$ and †$P \leq 0.05$ $Cc1^{-/-xliver+}$ versus $Cc1^{-/-}$ mice. (D) Heart lysates were analyzed by Western blot using caspase 3 antibody that detected the cleaved fragment of ~20 kDa apparent molecular weight. Gels represent 2 separate experiments performed on different mice/genotype/treatment.

Nox4, and *gp91* (Table S5). This could result in part from reduced PGE2 levels (Figure 1B*iv*), as reported [41,42]. Nonetheless, all oxidative stress markers were normalized in $Cc1^{-/-xliver+}$ mice (Figure 7C and Table S5).

Consistent with oxidative stress causing cardiomyocyte apoptosis, Western blot analysis revealed an increase in cleaved caspase 3 levels in the heart lysates of $Cc1^{-/-}$ relative to $Cc1^{+/+}$ mice, but was reversed in $Cc1^{-/-xliver+}$ mice (Figure 7D).

3.7. $Cc1^{-/-}$ mice manifest blunted insulin signaling in heart lysates

We then examined whether hyperinsulinemia-driven systemic factors affected insulin signaling in $Cc1^{-/-}$ heart in parallel to cardiac dysfunction. To this end, we assessed activation of insulin signaling pathway in the lysates of hearts removed from overnight fasted (F) and refed (RF) mice. Western blot analysis revealed lower IRβ protein level in $Cc1^{-/-}$ than $Cc1^{+/+}$ and $Cc1^{-/-xliver+}$ heart lysates (Figure 8A,

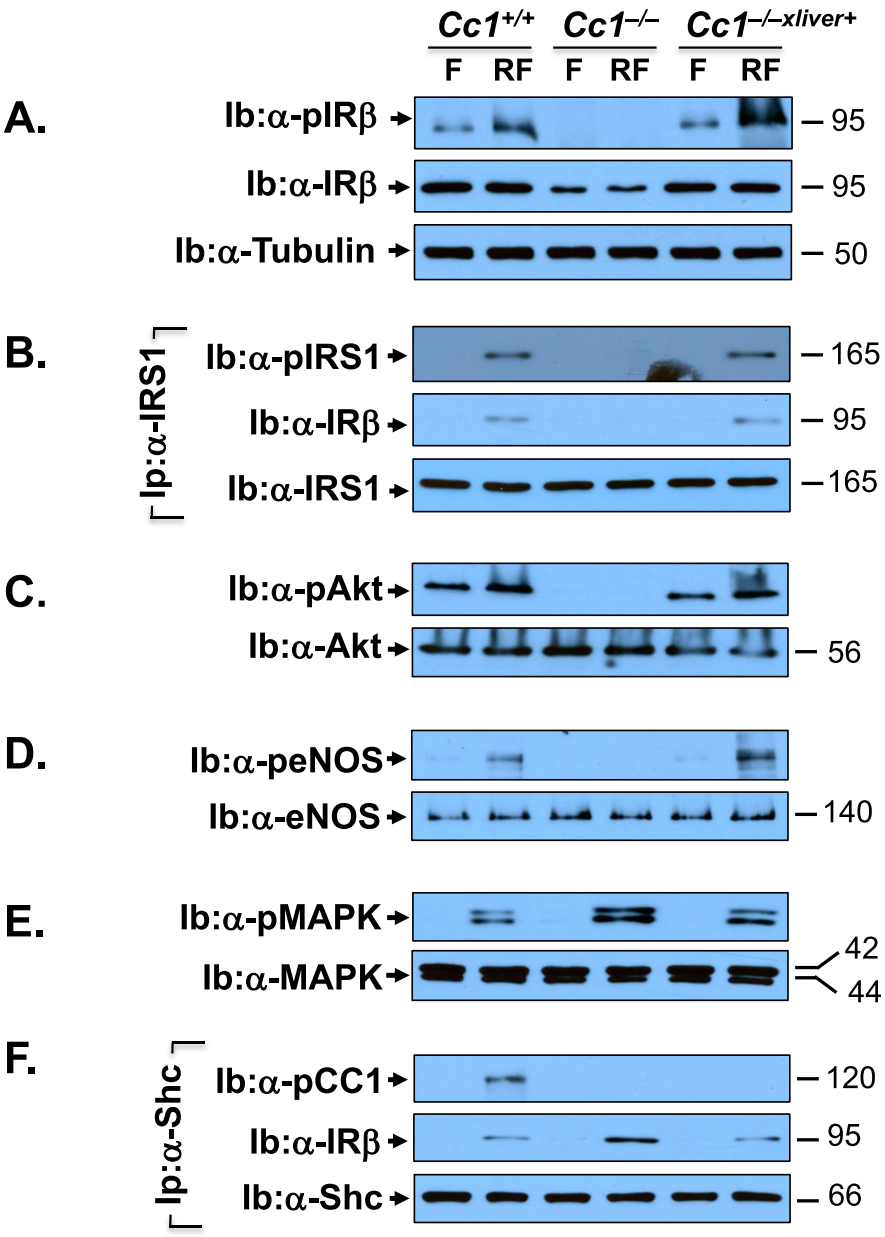

Figure 8: Insulin signaling in the heart. The hearts were removed from the same 8 month-old fasted (F) and refed (RF) mice as in Figure 4. Western analysis was performed by immunoblotting (Ib) with antibodies against phospho-IRβ (*A*, α-pIRβ), phospho-Akt (C, α-pAkt), phospho-eNOS (D, α-peNOS), and phospho-MAPKinase (E, α-pMAPK), in addition to immunoblotting (Ib) with antibodies against IRβ, Akt, eNOS, and MAPK, respectively for normalization. In (A), the lower half of the membrane was immunoblotted with α-tubulin to normalize against protein loading (lower gel). In (B), some aliquots were subjected to immunoprecipitation (Ip) with α-IRS1 antibody followed by immunoblotting wih α-phospho-IRS1 antibody (α-pIRS1, top gel), normalized to total IRS1 (lower gel). The immunopellet was also immunoblotted with α-pIRβ antibody to detect binding between IRS1 and IRβ (middle gel). In (F), a similar co-immunoprecipitation experiment was carried out to detect phospho-CEACAM1 (pCC1) (top gel) or IRβ (middle gel) in the Shc immunopellet. The apparent molecular weight (kDa) is indicated at the right hand-side of each gel. Gels represent more than two separate experiments performed on different mice/genotype/treatment group.

middle panel normalized to tubulin in the lower gel as marker of loaded protein). Consistently, insulin failed to induce IRβ phosphorylation in refed *Cc1*$^{-/-}$ hearts as it did to *Cc1*$^{+/+}$ and *Cc1*$^{-/-xliver+}$ mice, when compared to their fasting state (Figure 8A, top gel). Subsequently, insulin failed to phosphorylate (and activate) downstream IRS1/Akt/eNOS pathway in refed *Cc1*$^{-/-}$ hearts (Figure 8B–D). Together, this indicates that hyperinsulinemia contributes to dysregulated insulin-dependent activation of eNOS and subsequently, lower NO content in *Cc1*$^{-/-}$ hearts.

Like aortae, insulin induced MAPKinase phosphorylation to a larger extent in *Cc1*$^{-/-}$ than *Cc1*$^{+/+}$ and *Cc1*$^{-/-xliver+}$ hearts (Figure 8E), in parallel to a higher binding of Shc to IRβ in the Shc immunopellet (Ip) (Figure 8F, middle gel). This occurred in parallel to the reciprocal decrease in IRβ in the IRS1 immunopellet (Figure 8B, middle gel). The higher Shc-IRβ binding led to more coupling of the Ras/MAPkinase pathway to the receptor, and its higher activation to cause an increase in *Et-1* mRNA levels (Table S5) [2,4]. Moreover, *Etar* and *Etbr* mRNA levels and their *Etar*/*Etbr* ratio were ~5- to 7-fold higher in *Cc1*$^{-/-}$ hearts as compared to the other mouse groups (Table S5).

4. DISCUSSION

Insulin resistance is associated with cardiovascular abnormalities, including endothelial dysfunction, hypertension, and altered cardiac performance [10,43,44]. The role of hyperinsulinemia in the pathogenesis of endothelial dysfunction remains unclear. Fed a standard chow diet, *Cc1*$^{-/-}$ mice develop systemic insulin resistance at 5–6 months of age [15,16], and obesity in part due to leptin resistance [45]. Their vascular phenotype includes increased endothelial permeability and altered vascular remodeling [20,46], elevated systolic blood pressure [22], lower basal NO bioavailability and reduced vasodilatory response to acetylcholine in aortic rings [21], and plaque-like lesions in large vessels in the absence of hypercholesterolemia or a significant change in lipoprotein composition [21]. Together with the development of these abnormalities in the macrovasculature at >6 months of age, the current studies demonstrated that *Cc1*$^{-/-}$ mice also developed spontaneous endothelial dysfunction with cardiomyopathy and altered cardiac performance. This cardiovascular phenotype was reversed by liver-specific reconstitution of CEACAM1, which normalized hepatic insulin clearance and systemic insulin levels, followed by suppressing hepatic *de novo* lipogenesis and reversal of visceral obesity and lipolysis. This further assigns a key role for hyperinsulinemia-driven metabolic events in the pathogenesis of cardiovascular abnormalities in *Cc1*$^{-/-}$ mice.

In addition to low acetylcholine-induced endothelial dependent vasodilation of phenylephrine pre-contracted aortic rings [21], the current studies demonstrated reduced endothelium-dependent vasodilatory response of the resistance arterioles in *Cc1*$^{-/-}$ mice. The altered vasodilatory response to stimuli both in small and large conduit vessels could contribute to increased production of VCAM-1 and other cell adhesion molecules [33] that increase leukocyte adhesion to the endothelium, in addition to increased reactivity toward VCAM-1 [32,47]. Reversal of these abnormalities by liver-specific restoration of CEACAM1 expression suggests that they occurred, at least in part, as a consequence of hyperinsulinemia caused by *Ceacam1* deletion. For instance, chronic hyperinsulinemia activates the transcription of lipogenic genes, including *Fasn*, and prevents the suppressive effect of the acute rise of insulin on FASN activity to induce lipogenesis. This in turn, promotes fat redistribution from the liver to adipose tissue to cause visceral obesity and ensuing lipolysis and systemic pro-inflammatory state in *Cc1*$^{-/-}$ mice [48]. The rise in inflammatory markers such as TNFα could induce a direct upregulatory effect on VCAM-1 expression in *Cc1*$^{-/-}$ vessels [49–51], thus modulating leukocyte adhesion to the endothelium. The rise in plasma NEFA could activate both the vascular endothelium [52] and circulating leukocytes [53,54]. For instance, reduction in endothelial-dependent relaxation in *Cc1*$^{-/-}$ mice could result from elevated levels of plasma NEFA [55], which impair eNOS phosphorylation, independently of Akt-mediated signaling [56], and contribute to decreased NO production by reactive oxygen species-dependent mechanisms [57].

Cc1$^{-/-}$ mice also manifested altered cardiac performance with reduced left ventricular systolic function and left ventricular hypertrophy, consistent with the well documented association between obesity and left ventricular hypertrophy [38]. Moreover, recovery of the cardiac function in *Cc1*$^{-/-liver+}$ mice supports a significant role for systemic metabolic factors emanating from CEACAM1 deletion in liver in the cardiac phenotype of *Cc1*$^{-/-}$ mice, including increased lipogenesis in *Cc1*$^{-/-}$ hearts. Cardiac lipid accumulation could be caused by hyperinsulinemia-driven transcriptional induction of lipogenic genes, such as *Fasn* [17], as has been shown in patients with cardiomyopathy [58]. Together with elevated cardiac CD36 levels, which could mediate an increase in fatty acid uptake by endothelial cells and cardiomyocytes to promote lipid storage in the heart myocardium, this could contribute to inflammation, oxidative stress and cardiac dysfunction [59].

Curbing endothelial dysfunction and other cardiovascular abnormalities of *Cc1*$^{-/-}$ mice in response to restoring normo-insulinemia, insulin signaling, and lipid metabolism in the heart upon liver-specific rescuing of CEACAM1 underscores the significant role of hyperinsulinemia-driven lipid accumulation and insulin resistance in the pathogenesis of cardiovascular disease in *Ceacam1* null mice. This is supported by the notion that hyperinsulinemia constitutes an independent risk factor for vascular disease in humans [60], in part by causing an increase in ET-1 [61] and FASN levels [58]. Of note, hyperinsulinemia in the absence of insulin resistance, does not suffice to promote atherosclerosis in *ApoE*$^{-/-}$ mice with a monoallelic deletion of insulin receptors in endothelial cells that causes a reduction in insulin disposition [62]. Therefore, it is conceivable that hyperinsulinemia-driven insulin resistance and fat accumulation in endothelial aortae and hearts of *Cc1*$^{-/-}$ mice played a significant role in the pathogenesis of endothelial dysfunction and other cardiovascular abnormalities in these mice.

Mechanistically, we herein demonstrated that hyperinsulinemia caused downregulation of the insulin receptor in the aortae and heart lysates, reducing the phosphorylation of the insulin receptor and its IRS-1 substrate. The decrease in IRS-1 phosphorylation restricted Akt/eNOS/Foxo1 phosphorylation to reduce NO production in aortae and heart [4]. It also allowed for more Shc binding to the receptor to mediate coupling of the Ras/MAPKinase pathway followed by its activation and increased ET-1 transcription [2]. As has been reported in humans, this selective insulin resistance increased the *Etar*/*Etbr* ratio to disturb balance and mediated the vasoconstrictor function of ET-1 leading to endothelial dysfunction [61].

Moreover, fed hyperglycemia could contribute to increased oxidative stress and the cardiovascular abnormalities in *Cc1*$^{-/-}$ mice [63]. Given that these mice harbor most of the metabolic risk factors of cardiovascular disease associated with insulin resistance [64] that were eliminated by reconstituting CEACAM1 in the liver, we postulate that endothelial and cardiac dysfunctions in *Cc1*$^{-/-}$ mice were a primary cardiovascular consequence of hepatic-driven, sustained hyperinsulinemia and ensuing metabolic abnormalities.

5. CONCLUSION

In summary, the current study presents an *in vivo* demonstration of the link between metabolic and cardiovascular abnormalities in $Cc1^{-/-}$ mice. Reversal of the cardiovascular phenotype together with normalization of insulin levels and action in $Cc1^{-/-liver+}$ mice supports the role of hyperinsulinemia in regulating cardiovascular function [65,66] including the liver [67]. It is thus conceivable to predict that future therapy targeting hepatic CEACAM1 level and function may prove beneficial for the prevention of the cardiovascular disturbances that develop in metabolic syndrome.

FUNDING

This work was supported by grants from the National Institutes of Health [R01-DK-054254, R01-DK-083850, and R01-HL-112248 to S.M.N.; R01-HL-111877 to G.V.: DK-078757 and HL-091535 to H.M.S. and R01-DK-064344 to R.S]. It was also supported by fellowships from the American Heart Association [14POST20480294 to L.R. and 09POST2400144 to E.E.M.], and from the Middle-East Diabetes Research Center to H.E.G. The work was also supported by funds from the John J. Kopchick PhD OHF Eminent Research Chair endowment to S.M.N.

AUTHOR CONTRIBUTIONS

L.R. researched data and contributed to writing a first draft of the manuscript, H.T.M. researched data, optimized conditions to isolate cardiac primary cell isolations and contributed to the writing of a first draft of the manuscript and to its revision. H.E.G. researched data and critically reviewed the manuscript. A.M.W., E.E.M., S.S.Q., and G.P.L researched data. H.M.S. and G.V. designed experiments, discussed content and reviewed the manuscript. R.S. carried out endothelial function and leukocyte adhesion, analyzed data, and reviewed the manuscript. R.G designed, discussed and carried out echocardiography, analyzed data, and reviewed the manuscript. S.M.N. was responsible for study design, conceptualization, data analysis and results interpretation, and reviewing and completing the writing of the manuscript. S.M.N. had full access to all the data of the study and takes responsibility for the integrity and accuracy of data analysis and the decision to submit and publish the manuscript.

ACKNOWLEDGMENTS

The authors thank J. Kalisz and M. Kopfman at the Najjar Laboratory at the University of Toledo for their technical assistance in the generation, and maintenance of mice, and in carrying out routine RNA analyses.

CONFLICT OF INTEREST

None declared

APPENDIX A. SUPPLEMENTARY DATA

Supplementary data related to this article can be found at https://doi.org/10.1016/j.molmet.2018.01.009.

REFERENCES

[1] Petersen, K.F., Dufour, S., Savage, D.B., Bilz, S., Solomon, G., Yonemitsu, S., et al., 2007. The role of skeletal muscle insulin resistance in the pathogenesis of the metabolic syndrome. Proceedings of the National Academy of Sciences of the United States of America 104:12587–12594.

[2] Muniyappa, R., Montagnani, M., Koh, K.K., Quon, M.J., 2007. Cardiovascular actions of insulin. Endocrine Reviews 28:463–491.

[3] DeFronzo, R.A., Ferrannini, E., 1991. Insulin resistance. A multifaceted syndrome responsible for NIDDM, obesity, hypertension, dyslipidemia, and atherosclerotic cardiovascular disease. Diabetes Care 14:173–194.

[4] Kim, J.A., Montagnani, M., Koh, K.K., Quon, M.J., 2006. Reciprocal relationships between insulin resistance and endothelial dysfunction: molecular and pathophysiological mechanisms. Circulation 113:1888–1904.

[5] Mather, K.J., Steinberg, H.O., Baron, A.D., 2013. Insulin resistance in the vasculature. Journal of Clinical Investigation 123:1003–1004.

[6] Krieglstein, C.F., Granger, D.N., 2001. Adhesion molecules and their role in vascular disease. American Journal of Hypertension 14:44S–54S.

[7] Duncan, E.R., Crossey, P.A., Walker, S., Anilkumar, N., Poston, L., Douglas, G., et al., 2008. Effect of endothelium-specific insulin resistance on endothelial function in vivo. Diabetes 57:3307–3314.

[8] Kubota, T., Kubota, N., Moroi, M., Terauchi, Y., Kobayashi, T., Kamata, K., et al., 2003. Lack of insulin receptor substrate-2 causes progressive neointima formation in response to vessel injury. Circulation 107:3073–3080.

[9] Biddinger, S.B., Hernandez-Ono, A., Rask-Madsen, C., Haas, J.T., Aleman, J.O., Suzuki, R., et al., 2008. Hepatic insulin resistance is sufficient to produce dyslipidemia and susceptibility to atherosclerosis. Cell Metab 7:125–134.

[10] King, G.L., Park, K., Li, Q., 2016. Selective insulin resistance and the development of cardiovascular diseases in diabetes: the 2015 Edwin Bierman Award Lecture. Diabetes 65:1462–1471.

[11] Wheatcroft, S.B., Shah, A.M., Li, J.M., Duncan, E., Noronha, B.T., Crossey, P.A., et al., 2004. Preserved glucoregulation but attenuation of the vascular actions of insulin in mice heterozygous for knockout of the insulin receptor. Diabetes 53:2645–2652.

[12] Vicent, D., Ilany, J., Kondo, T., Naruse, K., Fisher, S.J., Kisanuki, Y.Y., et al., 2003. The role of endothelial insulin signaling in the regulation of vascular tone and insulin resistance. Journal of Clinical Investigation 111:1373–1380.

[13] Najjar, S.M., Philippe, N., Suzuki, Y., Ignacio, G.A., Formisano, P., Accili, D., et al., 1995. Insulin-stimulated phosphorylation of recombinant pp120/HA4, an endogenous substrate of the insulin receptor tyrosine kinase. Biochemistry 34:9341–9349.

[14] Choice, C.V., Howard, M.J., Poy, M.N., Hankin, M.H., Najjar, S.M., 1998. Insulin stimulates pp120 endocytosis in cells co-expressing insulin receptors. Journal of Biological Chemistry 273:22194–22200.

[15] DeAngelis, A.M., Heinrich, G., Dai, T., Bowman, T.A., Patel, P.R., Lee, S.J., et al., 2008. Carcinoembryonic antigen-related cell adhesion molecule 1: a link between insulin and lipid metabolism. Diabetes 57:2296–2303.

[16] Xu, E., Dubois, M.J., Leung, N., Charbonneau, A., Turbide, C., Avramoglu, R.K., et al., 2009. Targeted disruption of carcinoembryonic antigen-related cell adhesion molecule 1 promotes diet-induced hepatic steatosis and insulin resistance. Endocrinology 150:3503–3512.

[17] Osborne, T.F., 2000. Sterol regulatory element-binding proteins (SREBPs): key regulators of nutritional homeostasis and insulin action. Journal of Biological Chemistry 275:32379–32382.

[18] Lester, S.G., Russo, L., Ghanem, S.S., Khuder, S.S., DeAngelis, A.M., Esakov, E.L., et al., 2015. Hepatic CEACAM1 over-expression protects against diet-induced fibrosis and inflammation in white adipose tissue. Frontiers in Endocrinology (Lausanne) 6:116–122.

[19] Russo, L., Muturi, H.T., Ghadieh, H.E., Ghanem, S.S., Bowman, T.A., Noh, H.L., et al., 2017. Liver-specific reconstitution of CEACAM1 reverses the metabolic abnormalities caused by its global deletion in male mice. Diabetologia 60:2463–2474.

[20] Nouvion, A.L., Oubaha, M., Leblanc, S., Davis, E.C., Jastrow, H., Kammerer, R., et al., 2010. CEACAM1: a key regulator of vascular permeability. Journal of Cell Science 123:4221–4230.

[21] Najjar, S.M., Ledford, K.J., Abdallah, S.L., Paus, A., Russo, L., Kaw, M.K., et al., 2013. Ceacam1 deletion causes vascular alterations in large vessels. American Journal of Physiology. Endocrinology and Metabolism 305:E519—E529.

[22] Huang, J., Ledford, K.J., Pitkin, W.B., Russo, L., Najjar, S.M., Siragy, H.M., 2013. Targeted deletion of murine CEACAM 1 activates PI3K-Akt signaling and contributes to the expression of (Pro)renin receptor via CREB family and NF-kappaB transcription factors. Hypertension 62:317—323.

[23] Al-Share, Q.Y., DeAngelis, A.M., Lester, S.G., Bowman, T.A., Ramakrishnan, S.K., Abdallah, S.L., et al., 2015. Forced hepatic overexpression of CEACAM1 curtails diet-induced insulin resistance. Diabetes 64: 2780—2790.

[24] Najjar, S.M., Yang, Y., Fernstrom, M.A., Lee, S.J., Deangelis, A.M., Rjaily, G.A., et al., 2005. Insulin acutely decreases hepatic fatty acid synthase activity. Cell Metabolism 2:43—53.

[25] Ouedraogo, R., Gong, Y., Berzins, B., Wu, X., Mahadev, K., Hough, K., et al., 2007. Adiponectin deficiency increases leukocyte-endothelium interactions via upregulation of endothelial cell adhesion molecules in vivo. Journal of Clinical Investigation 117:1718—1726.

[26] Smedlund, K.B., Birnbaumer, L., Vazquez, G., 2015. Increased size and cellularity of advanced atherosclerotic lesions in mice with endothelial overexpression of the human TRPC3 channel. Proceedings of the National Academy of Sciences of the United States of America 112:E2201—E2206.

[27] Ackers-Johnson, M., Li, P.Y., Holmes, A.P., O'Brien, S.M., Pavlovic, D., Foo, R.S., 2016. A simplified, Langendorff-free method for concomitant isolation of viable cardiac myocytes and nonmyocytes from the adult mouse heart. Circulation Research 119:909—920.

[28] Lim, Y.C., Luscinskas, F.W., 2006. Isolation and culture of murine heart and lung endothelial cells for in vitro model systems. Methods in Molecular Biology 341:141—154.

[29] Aroor, A.R., Demarco, V.G., Jia, G., Sun, Z., Nistala, R., Meininger, G.A., et al., 2013. The role of tissue renin-angiotensin-aldosterone system in the development of endothelial dysfunction and arterial stiffness. Frontiers in Endocrinology (Lausanne) 4:161.

[30] Pelletier, S., Dube, J., Villeneuve, A., Gobeil Jr., F., Yang, Q., Battistini, B., et al., 2001. Prostaglandin E(2) increases cyclic AMP and inhibits endothelin-1 production/secretion by guinea-pig tracheal epithelial cells through EP(4) receptors. British Journal of Pharmacology 132:999—1008.

[31] Satitthummanid, S., Uaprasert, N., Songmuang, S.B., Rojnuckarin, P., Tosukhowong, P., Sutcharitchan, P., et al., 2017. Depleted nitric oxide and prostaglandin E2 levels are correlated with endothelial dysfunction in beta-thalassemia/HbE patients. International Journal of Hematology 106:366—374.

[32] Cybulsky, M.I., Iiyama, K., Li, H., Zhu, S., Chen, M., Iiyama, M., et al., 2001. A major role for VCAM-1, but not ICAM-1, in early atherosclerosis. Journal of Clinical Investigation 107:1255—1262.

[33] De Caterina, R., Libby, P., Peng, H.B., Thannickal, V.J., Rajavashisth, T.B., Gimbrone Jr., M.A., et al., 1995. Nitric oxide decreases cytokine-induced endothelial activation. Nitric oxide selectively reduces endothelial expression of adhesion molecules and proinflammatory cytokines. Journal of Clinical Investigation 96:60—68.

[34] Gomez-Hernandez, A., Perdomo, L., de las Heras, N., Beneit, N., Escribano, O., Otero, Y.F., et al., 2014. Antagonistic effect of TNF-alpha and insulin on uncoupling protein 2 (UCP-2) expression and vascular damage. Cardiovascular Diabetology 13:108.

[35] Cook, J.R., Langlet, F., Kido, Y., Accili, D., 2015. Pathogenesis of selective insulin resistance in isolated hepatocytes. Journal of Biological Chemistry 290: 13972—13980.

[36] Gustafson, T.A., He, W., Craparo, A., Schaub, C.D., O'Neill, T.J., 1995. Phosphotyrosine-dependent interaction of SHC and insulin receptor substrate 1 with the NPEY motif of the insulin receptor via a novel non-SH2 domain. Molecular and Cellular Biology 15:2500—2508.

[37] Wiernsperger, N., Nivoit, P., De Aguiar, L.G., Bouskela, E., 2007. Microcirculation and the metabolic syndrome. Microcirculation 14:403—438.

[38] Woodiwiss, A.J., Norton, G.R., 2015. Obesity and left ventricular hypertrophy: the hypertension connection. Current Hypertension Reports 17:539.

[39] Haemmerle, G., Moustafa, T., Woelkart, G., Buttner, S., Schmidt, A., van de Weijer, T., et al., 2011. ATGL-mediated fat catabolism regulates cardiac mitochondrial function via PPAR-alpha and PGC-1. Nature Medicine 17:1076—1085.

[40] Yu, Q., Lee, C.F., Wang, W., Karamanlidis, G., Kuroda, J., Matsushima, S., et al., 2014. Elimination of NADPH oxidase activity promotes reductive stress and sensitizes the heart to ischemic injury. Journal of the American Heart Association 3:e000555.

[41] Sanchez, A., Contreras, C., Villalba, N., Martinez, P., Martinez, A.C., Briones, A., et al., 2010. Altered arachidonic acid metabolism via COX-1 and COX-2 contributes to the endothelial dysfunction of penile arteries from obese Zucker rats. British Journal of Pharmacology 159:604—616.

[42] Hristovska, A.M., Rasmussen, L.E., Hansen, P.B., Nielsen, S.S., Nusing, R.M., Narumiya, S., et al., 2007. Prostaglandin E2 induces vascular relaxation by E-prostanoid 4 receptor-mediated activation of endothelial nitric oxide synthase. Hypertension 50:525—530.

[43] Frisbee, J.C., 2007. Vascular dysfunction in obesity and insulin resistance. Microcirculation 14:269—271.

[44] von Bibra, H., St John Sutton, M., 2010. Diastolic dysfunction in diabetes and the metabolic syndrome: promising potential for diagnosis and prognosis. Diabetologia 53:1033—1045.

[45] Heinrich, G., Russo, L., Castaneda, T.R., Pfeiffer, V., Ghadieh, H.E., Ghanem, S.S., et al., 2016. Leptin resistance contributes to obesity in mice with null mutation of carcinoembryonic antigen-related cell adhesion molecule 1. Journal of Biological Chemistry 291:11124—11132.

[46] Horst, A.K., Ito, W.D., Dabelstein, J., Schumacher, U., Sander, H., Turbide, C., et al., 2006. Carcinoembryonic antigen-related cell adhesion molecule 1 modulates vascular remodeling in vitro and in vivo. Journal of Clinical Investigation 116:1596—1605.

[47] Dansky, H.M., Barlow, C.B., Lominska, C., Sikes, J.L., Kao, C., Weinsaft, J., et al., 2001. Adhesion of monocytes to arterial endothelium and initiation of atherosclerosis are critically dependent on vascular cell adhesion molecule-1 gene dosage. Arteriosclerosis, Thrombosis, and Vascular Biology 21:1662—1667.

[48] Ghosh, S., Kaw, M., Patel, P.R., Ledford, K.J., Bowman, T.A., McLnerney, M.F., et al., 2010. Mice with null mutation of Ceacam I develop nonalcoholic steatohepatitis. Hepatic Medicine: Evidence and Research 2010: 69—78.

[49] Nishida, K., Otsu, K., 2017. Inflammation and metabolic cardiomyopathy. Cardiovascular Research 113:389—398.

[50] Zhang, J., Alcaide, P., Liu, L., Sun, J., He, A., Luscinskas, F.W., et al., 2011. Regulation of endothelial cell adhesion molecule expression by mast cells, macrophages, and neutrophils. PLoS One 6:e14525.

[51] Walker, T., Wendel, H.P., Tetzloff, L., Raabe, C., Heidenreich, O., Simon, P., et al., 2007. Inhibition of adhesion molecule expression on human venous endothelial cells by non-viral siRNA transfection. Journal of Cellular and Molecular Medicine 11:139—147.

[52] Shikama, Y., Aki, N., Hata, A., Nishimura, M., Oyadomari, S., Funaki, M., 2015. Palmitate-stimulated monocytes induce adhesion molecule expression in endothelial cells via IL-1 signaling pathway. Journal of Cellular Physiology 230: 732—742.

[53] Bunn, R.C., Cockrell, G.E., Ou, Y., Thrailkill, K.M., Lumpkin Jr., C.K., Fowlkes, J.L., 2010. Palmitate and insulin synergistically induce IL-6 expression in human monocytes. Cardiovascular Diabetology 9:73.

[54] Rodrigues, H.G., Takeo Sato, F., Curi, R., Vinolo, M.A., 2016. Fatty acids as modulators of neutrophil recruitment, function and survival. European Journal of Pharmacology 785:50—58.

[55] Steinberg, H.O., Tarshoby, M., Monestel, R., Hook, G., Cronin, J., Johnson, A., et al., 1997. Elevated circulating free fatty acid levels impair endothelium-dependent vasodilation. Journal of Clinical Investigation 100:1230—1239.

[56] Symons, J.D., McMillin, S.L., Riehle, C., Tanner, J., Palionyte, M., Hillas, E., et al., 2009. Contribution of insulin and Akt1 signaling to endothelial nitric oxide synthase in the regulation of endothelial function and blood pressure. Circulation Research 104:1085—1094.

[57] Edirisinghe, I., McCormick Hallam, K., Kappagoda, C.T., 2006. Effect of fatty acids on endothelium-dependent relaxation in the rabbit aorta. Clinical Science (London) 111:145—151.

[58] Semenkovich, C.F., 2017. We know more than we can tell about diabetes and vascular disease: the 2016 Edwin Bierman Award Lecture. Diabetes 66: 1735—1741.

[59] Abumrad, N.A., Goldberg, I.J., 2016. CD36 actions in the heart: lipids, calcium, inflammation, repair and more? Biochimica et Biophysica Acta 1860:1442—1449.

[60] Despres, J.P., Lamarche, B., Mauriege, P., Cantin, B., Dagenais, G.R., Moorjani, S., et al., 1996. Hyperinsulinemia as an independent risk factor for ischemic heart disease. New England Journal of Medicine 334:952—957.

[61] Mahmoud, A.M., Szczurek, M.R., Blackburn, B.K., Mey, J.T., Chen, Z., Robinson, A.T., et al., 2016. Hyperinsulinemia augments endothelin-1 protein expression and impairs vasodilation of human skeletal muscle arterioles. Physiological Reports 4.

[62] Rask-Madsen, C., Buonomo, E., Li, Q., Park, K., Clermont, A.C., Yerokun, O., et al., 2012. Hyperinsulinemia does not change atherosclerosis development in apolipoprotein E null mice. Arteriosclerosis, Thrombosis, and Vascular Biology 32:1124—1131.

[63] Shah, M.S., Brownlee, M., 2016. Molecular and cellular mechanisms of cardiovascular disorders in diabetes. Circulation Research 118:1808—1829.

[64] Rask-Madsen, C., King, G.L., 2013. Vascular complications of diabetes: mechanisms of injury and protective factors. Cell Metabolism 17:20—33.

[65] Sankaralingam, S., Abo Alrob, O., Zhang, L., Jaswal, J.S., Wagg, C.S., Fukushima, A., et al., 2015. Lowering body weight in obese mice with diastolic heart failure improves cardiac insulin sensitivity and function: implications for the obesity paradox. Diabetes 64:1643—1657.

[66] Jia, G., DeMarco, V.G., Sowers, J.R., 2016. Insulin resistance and hyperinsulinaemia in diabetic cardiomyopathy. Nature Reviews Endocrinology 12: 144—153.

[67] Magida, J.A., Leinwand, L.A., 2014. Metabolic crosstalk between the heart and liver impacts familial hypertrophic cardiomyopathy. EMBO Molecular Medicine 6:482—495.

